Copyright © 2007 Tech Science Press MCB, vol.4, no.3, pp.159-176, 2007

Two-Layer Passive/Active Anisotropic FSI Models with Fiber Orientation: MRI-Based Patient-Specific Modeling of Right Ventricular Response to Pulmonary Valve Insertion Surgery

Dalin Tang[*], **Chun Yang**[†], **Tal Geva**[‡§], **and Pedro J. del Nido**[¶]

Abstract: A single-layer isotropic patient-specific right/left ventricle and patch (RV/LV/Patch) combination model with fluid-structure interactions (FSI) was introduced in our previous papers to evaluate and optimize human pulmonary valve replacement/insertion (PVR) surgical procedure and patch design. In this paper, an active anisotropic model with two-layer structure for ventricle wall and tissue fiber orientation was introduced to improve previous isotropic model for more accurate assessment of RV function and potential application in PVR surgery and patch design. A material-stiffening approach was used to model active heart contraction. The computational models were used to conduct "virtual (computational)" surgeries and test the hypothesis that a PVR surgical design with a smaller patch and more aggressive scar tissue trimming would lead to improved RV cardiac function recovery. Results from our models validated by pre-operation data indicated that the small patch design had 11% improvement in RV function as measured by RV ejection fraction, compared to the conventional patch. Maximum Stress-P_1 value from the active anisotropic model was 121.2% higher than that from the passive isotropic model. Computational RV volume predictions agreed well with CMR-measured volume data (error < 2%).

Keyword: right ventricle, congenital heart disease, Tetralogy of Fallot, heart model, fluid-structure interaction.

1 Introduction

Recent advances in computational modeling, methods and computer technology have made it possible for computer-simulated procedures (virtual surgery) to be used in clinical decision-making process to replace empirical and often risky clinical experimentation to examine the efficiency and suitability of various reconstructive procedures in diseased hearts. Since fluid-structure interaction (FSI) definitely plays an important role in heart motion and mechanical and cardiac functions, isotropic right/left ventricle and patch (RV/LV/Patch) combination models with fluid-structure interactions were introduced in our previous papers [31, 39] to evaluate RV cardiac function and provide helpful mechanical flow and stress/strain analysis for surgical procedure and patch design. In this paper, anisotropic material properties, a two-layer ventricle structure with tissue fiber orientation, and a material-stiffening approach to model active heart contraction were added to our previous RV/LV/Patch FSI models for more accurate assessment of RV function and potential application in RV pulmonary valve replacement/insertion (PVR) surgery design and patch optimization.

Right ventricular dysfunction is a common cause of heart failure in patients with congenital heart defects and often leads to impaired functional capacity and premature death. Patients with repaired Tetralogy of Fallot (ToF), a congenital

---

[*] Corresponding author: Dalin Tang, Mathematical Sciences Department, Worcester Polytechnic Institute, Worcester, MA 01609, Phone: 508-831-5332, fax: 508-831-5824, e-mail: dtang@wpi.edu

[†] Mathematics Department, Beijing Normal University, Beijing, China

[‡] Department of Cardiology, Children's Hospital, Boston

[§] Department of Pediatric, Harvard Medical School, Boston, MA 02115 USA

[¶] Dept. of Cardiac Surgery, Children's Hospital, Boston. Harvard Medical School, Boston, MA 02115 USA

(a) A human heart

(b) RV with Patch and scar.

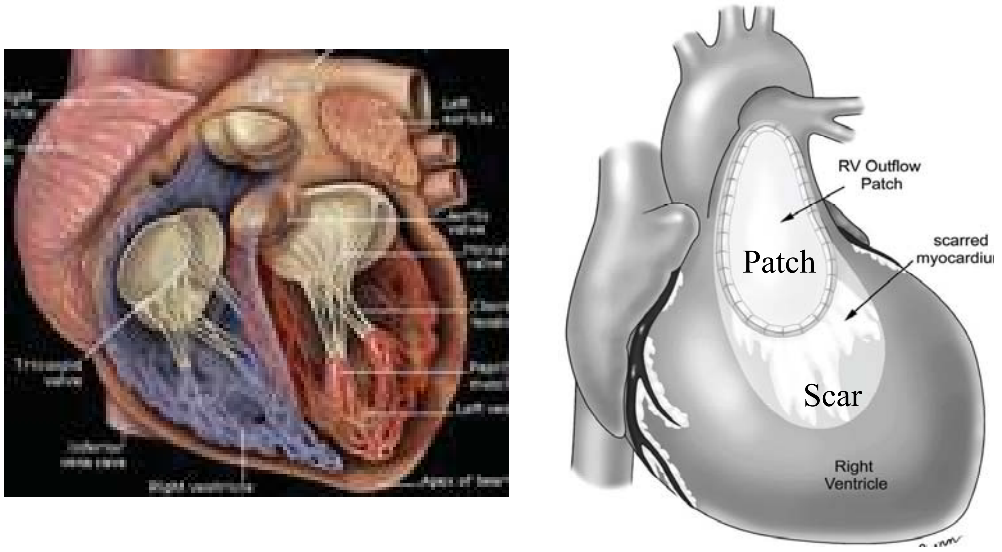

(c) Conventional Patch

(d) Small Patch

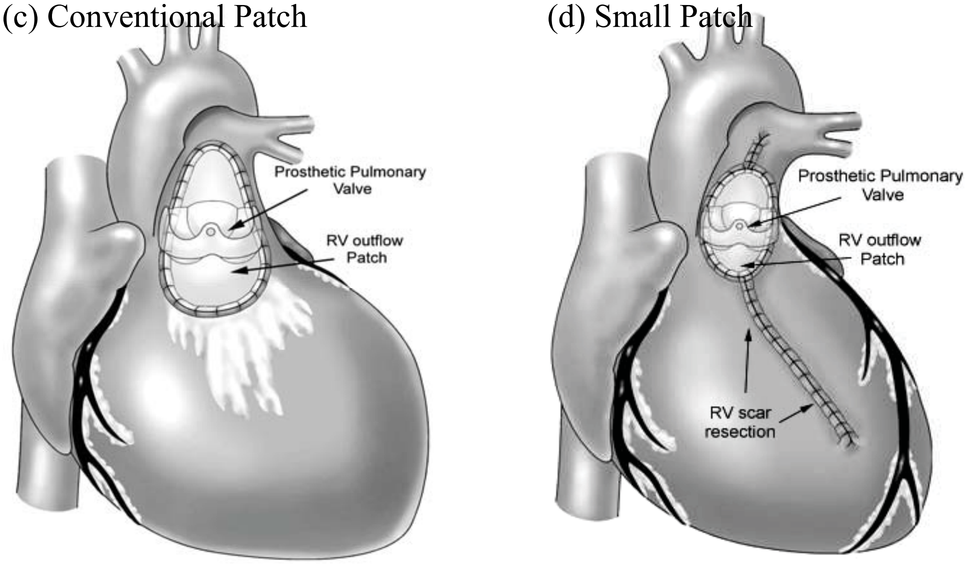

Figure 1: Repaired Tetralogy of Fallot heart with RV outflow patch and scar [7]. (a) Human heart; (b) RV with patch and scar; (c) Conventional patch; (d) Small patch with scar removal.

heart defect which includes a ventricular septal defect and severe right ventricular outflow obstruction, account for the majority of cases with late onset RV failure. The mechanism of failure is a complex interaction of chronic pulmonary valve regurgitation (present since the original repair), a non-contractile and sometimes aneurysmal RV outflow, ventricular scarring from the incision to remove RV outflow muscle at the original repair, and some residual obstruction to RV outflow. It is believed that mechanical factors play an important role in the development of the disease leading to RV failure. However, the exact mechanism as how mechanical forces and conditions would contribute to RV failure or recovery is currently unknown due to lack of available clinical data and patient-specific computational models. The current surgical approach, which includes pulmonary valve replacement/insertion (PVR), has yielded mixed results, with many of the patients seeing little if any improvement in RV function, while in others there is significant improvement [33, 39]. The reason for the unpredictable results is the fact that the PVR surgery only addresses one mechanism for RV dysfunction and dilatation, namely pulmonary regurgitation. More radical surgical procedures, where scar tissue and even non-contracting segments of the RV muscle are removed (see Fig. 1), are being performed [7]. However there is currently no mechanism for predicting which patients will benefit from the various surgical options, and certainly no mechanism for tailoring the procedure to the individual patient with some confidence of the outcome. We propose a novel surgical/modeling procedure to test the hypotheses that patient-specific image-based modeling can provide accurate information for assessment of RV function and that more aggressive scar removal using computer-aided surgery design with optimized post-operative RV morphology and patch design will lead to improved recovery of RV functions [7]. With the detailed flow and stress/strain solutions from the computational model with fluid-structure interactions, we hope to be able to better understand the mechanisms governing the disease development and the factors affecting the surgical outcome so that PVR procedure and patch design can be optimized.

Computational modeling and medical imaging technologies have made considerable advances in biological and clinical research in recent years [1, 5, 8-17, 19-26, 28-29, 32-33, 35-37]. In recent years, considerable effort has been devoted to quantifying heart tissue mechanical properties and fiber orientations mostly using animal models [6, 21, 24, 26, 30]. Humphrey's book provides a comprehensive review of the literature [15]. More recent efforts include introduction of MRI-based fluid-only or structure-only 3D models to investigate flow and stress/strain behaviors in the whole ventricle (either RV or LV) [8-12, 18-21, 25-26, 28-29, 35-36]. Stevens et al. introduced a 3D finite element solid model of the heart based on measurements of the geometry and the fiber and sheet orientations of pig hearts. The end-diastolic deformation of the model was computed using the "pole-zero" constitutive law to model the mechanics of passive myocardial tissue specimens. The sensitivities of end-diastolic fiber-sheet material strains and heart shape to changes in the material parameters were investigated [28-29]. McCulloch et al. performed extensive research for 3D ventricular geometry and myofiber architecture of the rabbit heart. Their work and their *Continuity* package included experimental and modeling studies of 3D cardiac mechanics and electrophysiology [18-20, 35-36]. In a series of papers, Guccione et al. introduced anisotropic passive and active ventricle models where an additional tension term was added to the stress field to model active heart contractions RV [8-12]. The work of Nash and Hunter [21] and Hunter et al. [16] has provided comprehensive reviews for heart modeling, including tissue properties, fiber orientation, passive and active mechanical models, electromechanical models, and whole heart models. Those animal models provide insight for human heart mechanics and function.

Due to the complexity of human heart structure, nonlinear anisotropic tissue material properties, and difficulties involved in acquiring human subject data and solving models including fluid–structure interactions (FSI), patient-specific RV models with FSI are lacking in the current literature. Early 3D models for blood flow in the heart include Peskin's model which introduced fiber-based LV model and the celebrated immersed-boundary method to study blood flow features in an idealized geometry with fluid-structure interactions [22-23]. Our recent papers [31, 39] introduced FSI RV/LV/Patch combination models based on patient-specific MRI data with healthy and diseased RV to perform computational simulations for surgery design and patch optimization. While the isotropic FSI models were able to provide accurate RV volume predictions, it is well-known that heart ventricles have multi-layer structure and that heart muscle demonstrates clear anisotropic material properties. Computational predictions for heart deformation and stress/strain predictions could be improved if anisotropic material properties and fiber orientation could be included in the model.

In this paper, passive and active 3D CMR-based RV/LV/Patch combination models which include a) fluid-structure interactions, b) anisotropic material properties, c) two-layer construction with myocardial fiber orientation are introduced to provide accurate assessment for RV mechanical conditions and cardiac function. Active ventricle contraction was modeling by a material stiffening approach. Both passive and active models were validated by pre- and post-surgery CMR data and then used to assess and optimize RV remodeling surgical procedures and RV outflow patch design with the ultimate goal of improving recovery of RV function after surgery. Details are given below.

2 Data acquisition, computational models, and solution procedures

CMR data was first acquired and segmented to get RV/LV geometries. Valve and patch positions were determined with flow data, delayed enhancement CMR to delineate location and extent of scar/patch, and the intra-operative observations of Dr. del Nido. The computational mesh and finite element model were generated based on RV/LV geometries, valve locations and patch design. The complete LV/RV/Patch FSI model was solved by ADINA (ADINA R&D, Watertown, MA, USA) using unstructured finite elements and the Newton-Raphson iteration method. Nonlinear incremental iterative procedures were used to handle fluid-structure interactions. ADINA is a well-tested commercial finite-element package and has been used by Tang et al. extensively to solve FSI models in the past 10 years [31-33, 39]. More details for the solution methods can be found in [2-3].

2.1 Data acquisition

Cardiac MRI (CMR) studies were performed by Dr. Tal Geva to acquire patient-specific ventricle geometry, heart motion, flow velocity, and flow rate for patients needing RV remodeling and pulmonary valve replacement operations before and after scheduled surgeries. 30 positions of the RV/LV were acquired during one cardiac cycle, with each position containing 10-14 planar slices. 3D RV/LV geometry and computational mesh were constructed following the procedures described in [31, 39]. Fig. 2 shows one set of pre-operation CMR images from a patient and segmented contours. Fig. 3 shows the stacked contours, RV/LV inner/outer surface plot, valve and patch positions, and two patch models modified from the pre-operative geometry for computational mechanical analysis. The patch models were constructed under guidance from Dr. del Nido with surgical limitations taken into consideration.

2.2 The fluid model

Blood flow in the right ventricle was assumed to be laminar, Newtonian, viscous and incompressible. The Navier-Stokes equations with ALE formulation were used as the governing equations. Pressure conditions were prescribed at the tricuspid (inlet) and pulmonary (outlet) valves (see Fig. 4 and [4, 17]). Since RV muscle was treated as passive material, pressure conditions were modified so that RV could be inflated properly by fluid forces. To simplify the computational model, the cardiac cycle was split into two phases: **a)** The filling phase when blood flows into RV, the inlet was open and the outlet was closed; **b)** The ejection phase when blood was ejected out of RV, the outlet was kept open and the inlet was closed. When the inlet or outlet was closed, flow velocity was set to zero and pressure was left unspecified. No-slip boundary conditions and natural force boundary conditions were specified at all interfaces to couple fluid and structure models together [2-3]. The fluid model is given below:

$$\rho(\partial \mathbf{u}/\partial t + ((\mathbf{u}-\mathbf{u}_g)\cdot\nabla)\mathbf{u}) = -\nabla p + \mu\nabla^2\mathbf{u}, \quad (1)$$

$$\nabla\cdot\mathbf{u} = 0, \quad (2)$$

$$\mathbf{u}|_\Gamma = \partial x/\partial t, \quad \partial\mathbf{u}/\partial n|_{\text{inlet, outlet}} = 0, \quad (3)$$

$$P|_{\text{inlet}} = p_{\text{in}}(t), (\text{inlet open}),$$

$$\mathbf{u}|_{\text{inlet}} = 0, (\text{inlet closed}), \quad (4)$$

$$P|_{\text{outlet}} = p_{\text{out}}(t), (\text{outlet open}),$$

$$\mathbf{u}|_{\text{outlet}} = 0, (\text{outlet closed}), \quad (5)$$

(a) Pre-Operation CMR images from a patient, End of Systole

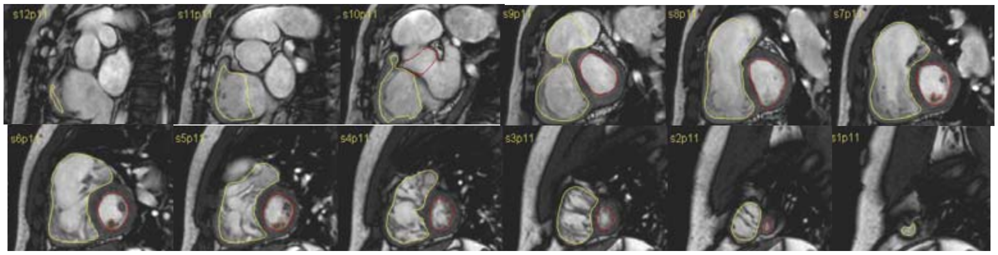

(b) Segmented Contours of RV-LV for Model Construction

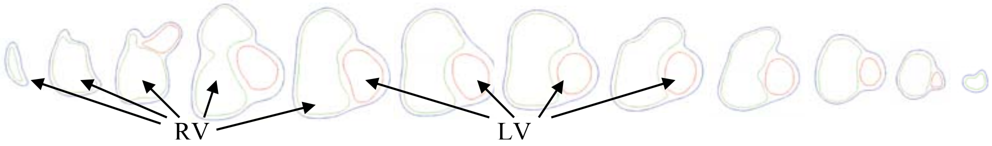

Figure 2: Pre-operation MR images (end-systole) acquired from a patient and segmented RV/LV contours for 3D geometry re-construction.

(a) Segmented RV/LV Contours (b) RV-LV Geometries (c) Inflated Whole Model, Strain-P_1 shown

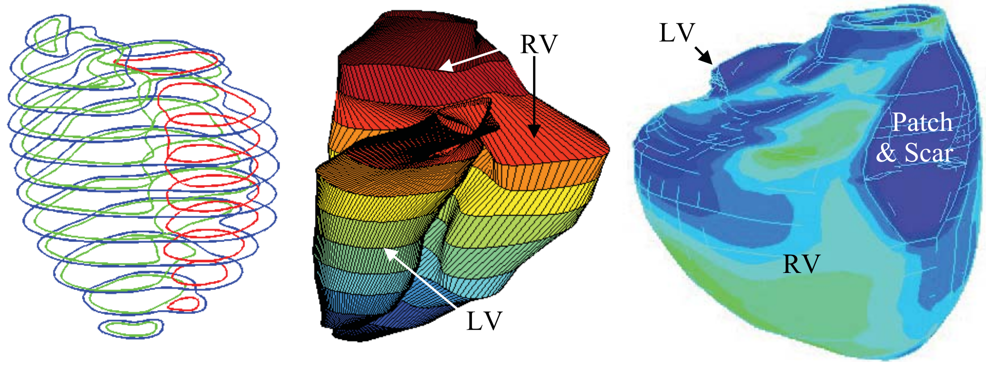

(d) Pre-Op Model with Old Patch and Scar Tissue. (e) Patch Model 1: Conventional Patch, Minimum Trimming. (f) Patch Model 2: a Small Patch and Aggressive Trimming.

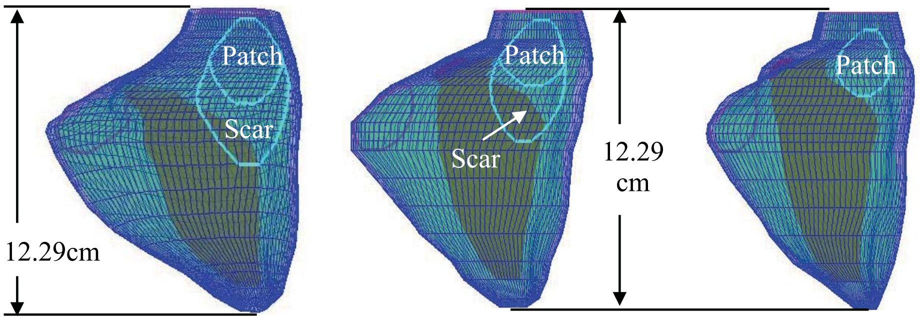

Figure 3: The 3D geometry re-construction process, conventional patch and proposed small patch models with patch locations.

$$p|_{\mathrm{LV}} = p_{\mathrm{LV}}(t), \tag{6}$$

$$\sigma_{ij} \cdot n_j|_{out\_wall} = 0, \tag{7}$$

$$\sigma^r_{ij} \cdot n_j|_{\mathrm{interface}} = \sigma^s_{ij} \cdot n_j|_{\mathrm{interface}}, \tag{8}$$

where $\mathbf{u}$ and p are fluid velocity and pressure, $\mathbf{u}_g$ is mesh velocity, Γ stands for RV inner wall, $f\bullet_{,j}$ stands for derivative of f with respect to the jth variable.

2.3 The passive anisotropic solid model

The RV and LV materials were assumed to be hyperelastic, anisotropic, nearly-incompressible and homogeneous. Isotropic RV/LV models introduced in our earlier papers were also solved for comparison purposes. Scar tissue and patch material were assumed to be hyperelastic, isotropic, nearly-incompressible and homogeneous. The governing equations for the structure models are:

$$\rho v_{i,tt} = \sigma_{ij,j}, \quad i,j = 1,2,3; \text{ sum over } j, \tag{9}$$

$$\varepsilon_{ij} = (v_{i,j} + v_{j,i} + v_{\alpha,i}v_{\alpha,j})/2, \quad i,j,\alpha = 1,2,3, \tag{10}$$

where σ is the stress tensor, ε is the strain tensor, v is solid displacement vector, $f\bullet_{,j}$ stands for derivative of f with respect to the jth variable, and ρ is material density. Equations (9)-(10) are used for RV/LV muscle, patch, and scar tissue.

The nonlinear Mooney-Rivlin model was used to describe the nonlinear anisotropic and isotropic material properties of the material with parameter values chosen to match experimental data available and adjusted to reflect stiffness variation of different materials [15, 19, 26]. The strain energy function for the isotropic modified Mooney-Rivlin model is given by [2-3, 31, 39]:

$$W = c_1(I_1-3) + c_2(I_2-3) + D_1[\exp(D_2(I_1-3))-1], \tag{11}$$

where I_1 and I_2 are the first and second strain invariants given by,

$$I_1 = \sum C_{ii}, \quad I_2 = 1/2[I_1^2 - C_{ij}C_{ij}], \tag{12}$$

$C = [C_{ij}] = X^T X$ is the right Cauchy-Green deformation tensor, $X = [X_{ij}] = [\partial x_i/\partial a_j]$, (x_i) is current position, (a_i) is original position, c_i and D_i are material parameters chosen to match experimental measurements [15,19,26]. The strain energy function for the anisotropic modified Mooney-Rivlin model anisotropic model was obtained by adding an additional anisotropic term in Eq. (3):

$$W = c_1(I_1-3) + c_2(I_2-3) + D_1[\exp(D_2(I_1-3))-1] + \frac{K_1}{2K_2}\exp[K_2(I_4-1)^2-1], \tag{13}$$

where $I_4 = C_{ij}(\mathbf{n}_f)_i(\mathbf{n}_f)_j$, C_{ij} is the Cauchy-Green deformation tensor, $\mathbf{n}_f$ is the fiber direction, K_1 and K_2 are material constants [13]. Parameter values in (13) can be chosen to fit the material models given in [19-20]:

$$W = \frac{C}{2}(e^Q - 1), \tag{14}$$

$$Q = b_1E_{ff}^2 + b_2(E_{cc}^2 + E_{rr}^2 + E_{cr}^2 + E_{rc}^2) + b_3(E_{fc}^2 + E_{cf}^2 + E_{fr}^2 + E_{rf}^2), \tag{15}$$

where E_{ff} is fiber strain, E_{cc} is cross-fiber inplane strain, E_{rr} is radial strain, and E_{cr}, E_{fr} and E_{fc} are the shear components in their respective coordinate planes, C, b_1, b_2, and b_3 are parameters to be chosen to fit experimental data. The 3D stress/strain relations can be obtained by finding various partial derivatives of the strain energy functions with respect to proper variables (strain/stretch components). Choosing c_1 = 0.351 KPa, c_2 = 0, D_1 = 0.0633 KPa, D_2 = 5.3, K_1 = 1.913 KPa, K_2 = 6.00 in (13). Fig. 5 shows our model agrees very well with the model given in [19-20]. The patient-specific stress-stretch curves derived from the modified Mooney-Rivlin models fitting CMR-measured data are given by Fig. 6.

2.4 Active anisotropic material model

Modeling active heart contraction is much harder because stress in a pumping human heart cannot be measured in vivo non-invasively (at least not with available technology in current practice). Heart expansion/contraction can be considered as combination of passive elastic expan-

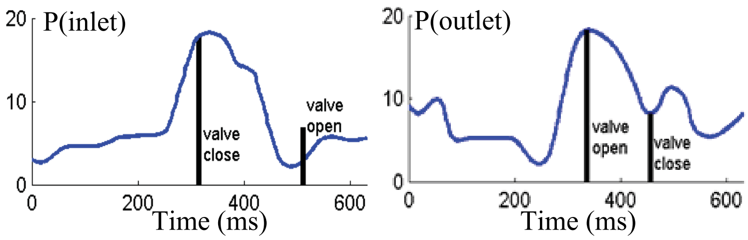
(a) Recorded Tricuspid Valve Pressure

(b) Recorded Pulmonary Valve Pressure

(c) Numerical Valve Pressure Conditions

(d) Patient-Specific Pressure Conditions

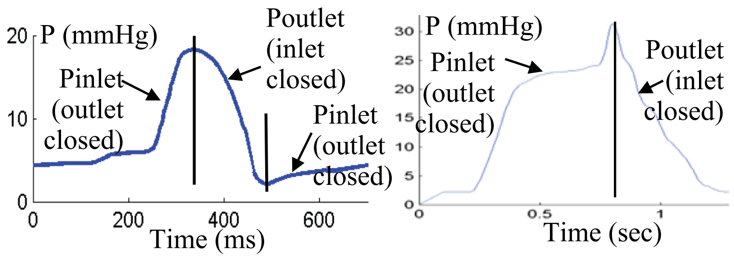

Figure 4: Recorded and prescribed pressure conditions at the tricuspid (inlet) and pulmonary (outlet) valves [4, 17]. Prescribed numerical pressure conditions and valve close/open times were modified from the recorded data so that pressure conditions were as consistent with the recorded data as possible. The vertical bars in (c)-(d) indicate valve open/close switch time.

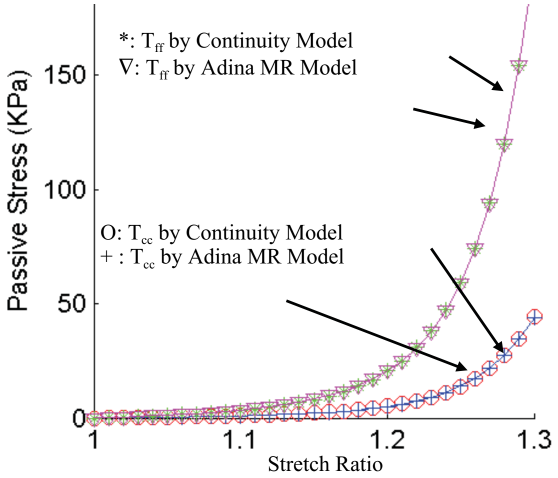

Figure 5: Anisotropic Mooney-Rivlin Model matches well with the model in the Continuity package [19]. Parameters used for the Adina MR-model: $c_1 = 0.351$ KPa, $c_2 = 0$, $D_1 = 0.0633$ KPa, $D_2 = 5.30$, $K_1 = 1.913$ KPa, $K_2 = 6.00$.

sion/contraction caused by blood pressure and active contraction/relaxation caused by fiber stiffening/relaxation. Fluid-structure interaction plays an important role in the process. During the filling phase, increase of RV blood pressure causes passive elastic expansion of the ventricle, accompanied by RV fiber relaxation. In the ejection phase, RV material stiffens and leads to ejection; at the same time, RV blood pressure decrease also leads to (passive) elastic ventricle contraction. The stress/strain distributions (passive and active combined) are determined by mechanical conservation laws (9)-(10) with proper boundary conditions and material constitutive laws. Since it is very hard to separate and measure the passive and active stresses/strains in clinical practice, we chose to specify time-dependent material stiffness parameters to model RV tissue stiffening and active RV contraction. RV muscle fibers will contract/relax by following a time-dependent stiffening/relaxation material model. The time-dependent material parameters in (13) will be adjusted to match CMR-measured patient-specific pressure-volume values. Fig. 6 shows our passive isotropic and anisotropic stress-stretch curves

(Fig. 6(a)) and end diastolic/systolic stress-stretch curves for the active anisotropic model (Fig. 6(b)). The time-dependent stiffness parameters in Eq. (13) (each parameter in (5) was a function of time) were numerically determined to match CMR measured RV volume curves.

2.5 *Two-layer model with fiber orientation*

As patient-specific fiber orientation data is not yet available in current practice, we chose to construct a two-layer RV/LV model and set fiber orientation angles using fiber angles given in Hunter [16] (see Fig. 7). The angles can be adjusted in our model easily volume by volume (the segment between two slices are divided into several blocks called "volumes" in ADINA so that proper mesh can be generated when patient-specific fiber orientation data becomes available [27]. Fig. 7 shows fiber orientations on a patient-specific RV/LV model and a segment of the two-layer model between two slices. Fiber orientation data from [27] indicated that fiber orientations in human heart follow similar patterns as shown in Fig. 7.

2.6 *LV model*

For simplicity, LV is included as a structure-only model with the same material parameter values used as those used for RV tissues. Inclusion of LV provides structure support for the part of RV surface connected to LV. This is important to obtain the correct RV motion and deformation. Blood flow in the LV was not included to reduce the size of the computational code and total CPU time. A recorded LV pressure was specified so that the LV will deform properly [4].

2.7 *Simulation procedures*

Equations (1)-(13) give the complete FSI model, with proper initial and boundary flow, pressure and stress/strain conditions. We start our simulation cycle when RV has its smallest volume (end of systole) corresponding to the minimal inlet pressure. As the inlet pressure increases (inlet is kept open), blood flows into RV and its volume increases. When RV reaches its maximal volume, the tricuspid valve closes and the pulmonary valves opens up. Blood is ejected and RV volume decreases. That completes the cycle. While the mechanism driving the motion is different from the real actively-contracting heart, our simulated RV motion, deformation, volume change, ejection fraction and fluid flow can provide results matching patient-specific volume data with properly-adjusted material parameters and flow-pressure boundary conditions.

3 Results

3.1 *Comparison of passive isotropic/anisotropic and active anisotropic models*

Nine fully-coupled FSI RV/LV combination models (the pre-operation model called M1, Patch Model 1 called M2 for conventional patch, Patch Model 2 called M3 with small patch and aggressive trimming, each with passive isotropic/anisotropic and active anisotropic material properties) were solved by ADINA to obtain full 3D flow, RV deformation and stress-strain distributions for detailed mechanical analysis and comparative studies. Fig. 8 gives a cut-surface and selected stress/strain plots given by the active anisotropic pre-operation model corresponding to maximum and minimum pressure conditions. Maximum stress values were found to be closely related to RV curvature and wall thickness, less influenced by stiffness variations among RV tissue, scar and patch materials. Maximum principal strain (Strain-P_1) distributions demonstrated closer link to stiffness changes, as shown by Figures 8(c) and (e). Fig. 9 gives selected Stress-P_1 and Strain-P_1 plots from the passive isotropic and anisotropic pre-operation models. Maximum Stress-P_1 values corresponding to maximum RV pressure from the passive isotropic, passive anisotropic, and active anisotropic models were 359.8, 898, and 796 KPa respectively. The stress values from passive and active anisotropic models were 149.6% and 121.2% higher than those from the passive isotropic model, respectively. This supports the use of the anisotropic multi-layer models which give more accurate stress predictions [14]. Maximum Strain-P_1 values from the

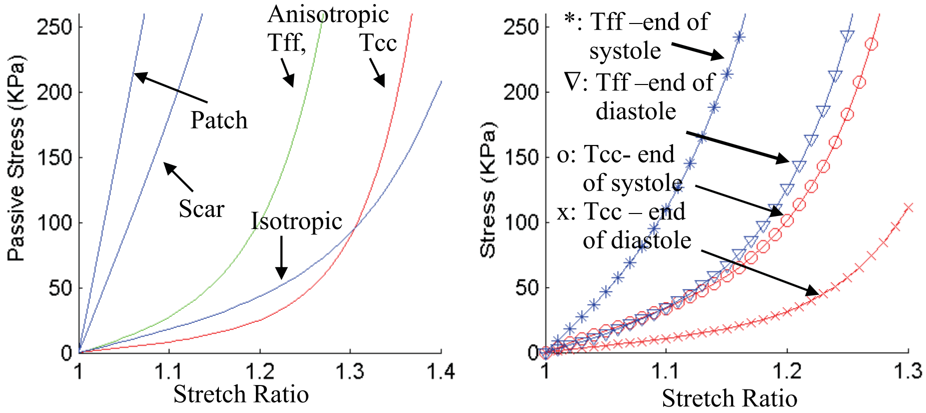
(a) Stress-stretch curves for passive

(b) Stress-stretch curves from proposed patient-

Figure 6: Stress-Stretch curves from isotropic and passive and active anisotropic models used in this paper. Model parameter values were selected to match CMR pressure-volume data: Isotropic RV tissue: c_1=7.36 KPa, c_2=0, D_1=2.88 KPa, D_2=4.0; Scar: c_1=73.6 KPa, c_2=0, D_1=28.8 KPa, D_2=4.0; Patch: c_1=147.2 KPa, c_2=0, D_1=57.6 KPa, D_2=4.0; Anisotropic Continuity model [17] parameters: C=18.04 KPa, b_1=8.79, b_2 =1.70, b_3=0.774. (b) End-systolic and end-diastolic T_{ff} and T_{cc} plots from proposed active patient-specific RV/LV model. End-systolic model parameters: C=72.16 KPa, b_1=8.79, b_2 =1.70, b_3=0.774; End-diastolic model parameters: C=22.55 KPa, b_1=8.79, b_2 =1.70, b_3=0.774.

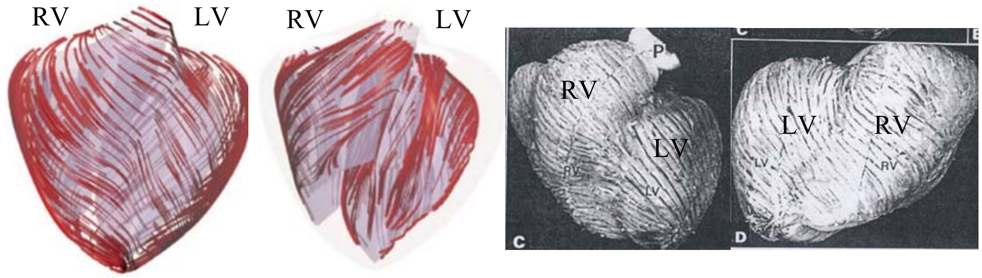
(a) Pig Model, Epicardium

(b) Pig Model, Endocardium

(c) Human Heart, Front View

(d) Human Heart, Back View

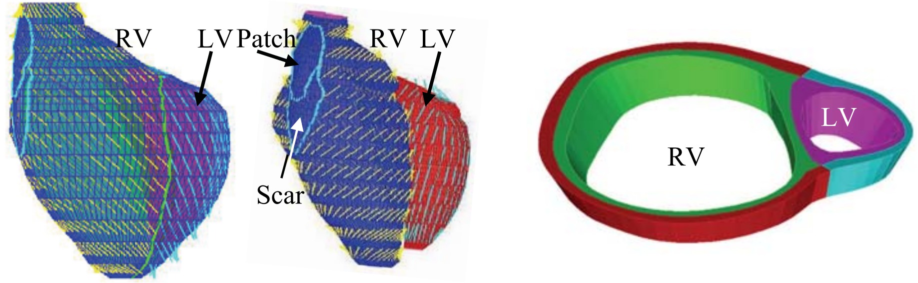
(e) Patient Model, Epicardium

(f) Patient Model, Endocardium.

(g) Model Construction Illustrations..

Figure 7: Fiber orientations from a pig model (Ref) and our patient-specific model. Fiber orientations are illustrated (a) on the epicardium, pig, (b) on the endocardial surfaces. LV fiber orientation is approximately -60° (relative to the circumferential direction) at the epicardium, and +80° at the endocardium. (c)-(d) Human ventricle fiber orientation from a patient; (e)-(f) Fiber orientation from our proposed RV/LV model based on patient-specific RV/LV morphologies. RV fiber orientation was set -45° at the epicardium, and +40° at the endocardium. The angles can be adjusted to fit patient-specific data. (g) Model construction illustrated using two slices.

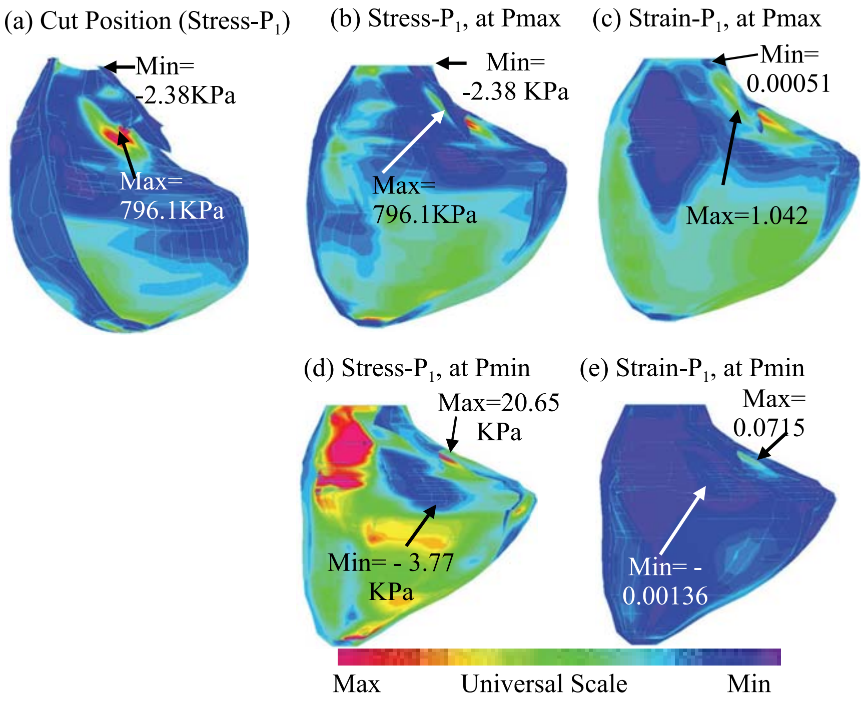

Figure 8: Selected cut-surface and Stress-P_1 and Strain-P_1 plots from the active anisotropic model at Pmax (beginning of ejection pahse) and Pmin (beginning of filling phase) conditions.

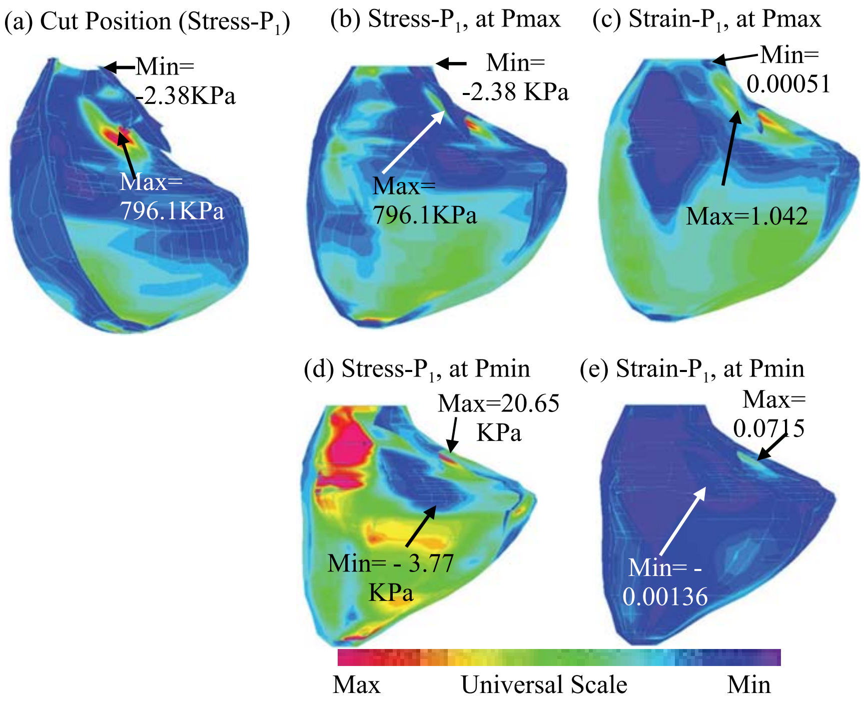

Figure 9: Model comparison: selected Stress-P_1 and Strain-P_1 plots from the passive isotropic and anisotropic models showing considerable differences in predicted stress/strain values.

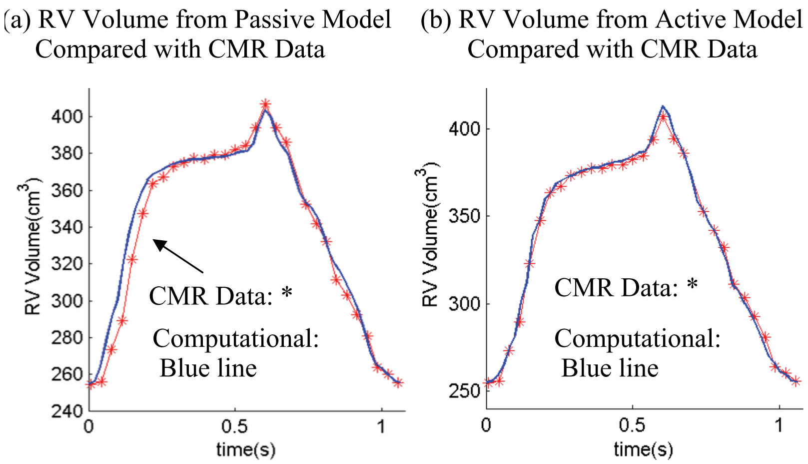
(a) RV Volume from Passive Model Compared with CMR Data

(b) RV Volume from Active Model Compared with CMR Data

Figure 10: Computed RV volumes from passive and active anisotropic pre-operation models compared with CMR recorded data showing good agreement (error margin < 2% for the active model). The active model has better agreement with CMR data because the material stiffness was adjusted for every time step to match with CMR volume data.

(a) Filling Phase (b) Ejection Begins (c) Ejection Continues

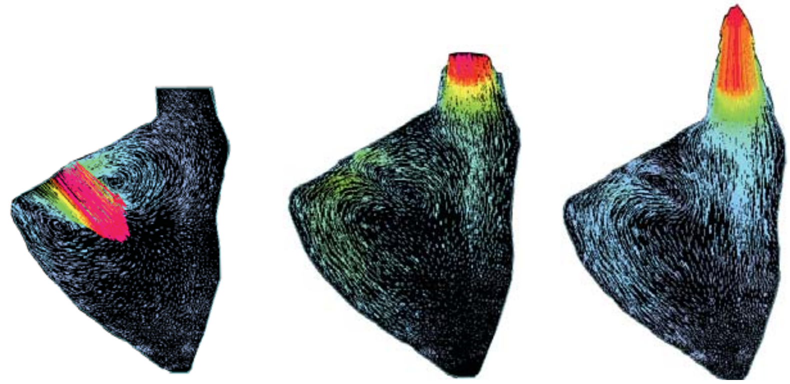

(d) Filling Phase (e) Ejection Begins (f) Ejection Continues

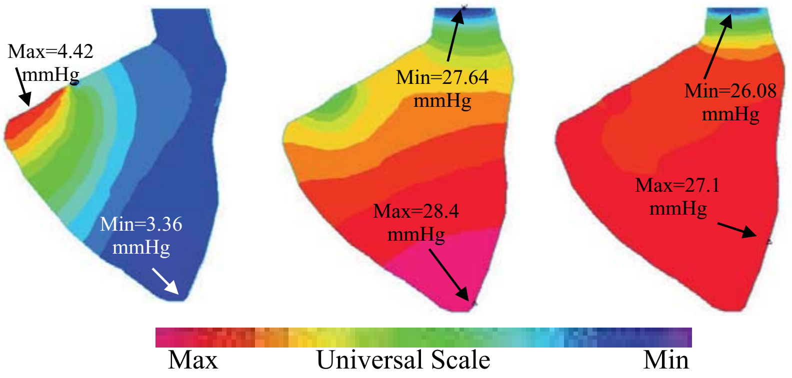

Figure 11: Flow velocity and pressure band plots during the filling and ejection phases showing interesting patterns.

active model were lower than those from the passive models. Localized stress/strain behaviors at selected sites will be tracked and presented later.

Fig. 10 shows that the computed RV volumes from both passive and active anisotropic models agreed well with CMR data. The model with active contraction gave more accurate predictions (error margin < 2% for the active model) because the material stiffness in the active model was adjusted for every time step to match with CMR volume data.

Fig. 11 gives some interesting flow patterns and pressure band plots in the filling-ejection cycle from M2. At the beginning of the filling phase, pressure at the inlet is higher than the inside pressure, blood is pumped into the ventricle (Fig. 11 (a) and (d)). The filling continues until the inlet closes, the outlet opens, and the ejection phase begins (Fig. 11 (b) and (e)). As ejection continues, the ventricle contracts, more blood is pumped out of the ventricle (Fig. 11 (c) and (f)). Pressure contour plots on the cut-surface corresponding to the velocity plots are given showing that maximum pressure was found near the inlet at the beginning of the filling phase. During the ejection phase, minimum pressure was found at the outlet as expected.

3.2 Assessment of RV Cardiac Function and Patch Model Comparisons

Based on the results and comparisons given in Section 3.1, the active anisotropic model was used to perform RV cardiac function assessment for the three patch models (M1, M2, and M3 as defined in 3.1) under consideration. Two major measures of RV cardiac function are stroke volume (SV) and ejection fraction (EF) defined as:

$$\begin{aligned} \text{SV} = {} & \text{RV End Diastolic (maximal) Volume} \\ & - \text{RV End Systolic (minimal) Volume,} \end{aligned} \tag{16}$$

$$\begin{aligned} \text{EF} = {} & [\text{RV end diastolic volume(RVEDV)} \\ & - \text{RV end systolic volume (RVESV)}]/\text{RVEDV,} \end{aligned} \tag{17}$$

RVEDV, RVESV, SV and EF values for M1, M2, and M3 are summarized in Table 1 which indicates that the proposed small patch model (M3) would provide about 11% improvement in EF, compared to the conventional patch model (M2). The fact that EF values for M1 and M2 were almost the same makes people wondering if the RV surgery brings any improvement for RV cardiac function. It should be noted that SV from the pre-op model is not a good measure of RV function because a considerable amount of blood leaks back through the pulmonary valve due to pulmonary regurgitation which is the reason for a PVI surgery. Fig. 12 gives CMR-measured accumulated out-flow volume at the pulmonary valve for M1. With pulmonary regurgitation taken into consideration, the adjusted EF value for M1 is only 18.1%. The computer-predicted EF improvement of M2 and M3 over M1 were 104% and 126.5%, respectively, when pulmonary regurgitation is taken into consideration. This is an important finding since the implication is that valve insertion alone has a greater relative benefit (104%) compared to the remodeling (an additional 22.5%). This needs to be validated by clinical studies with both pre- and post-operation data.

3.3 Smaller Patch leads to Reduced Stress Conditions in the Patch Area

To investigate mechanical conditions and stress/strain behaviors in the patch area, stress/strain values were tracked and Fig. 13 gives Stress-P_1 and Strain-P_1 variations tracked at selected locations for the pre-operation model (M1), the conventional patch model (M2), and the small patch model (M3). Our tracking results indicated that stress/strain levels around the patch were considerably lower from the small patch model compared to the conventional large patch model. Reduced stress/strain levels around the patch may be desirable for improved RV function and to prevent scarring of peri-patch myocardium, and should be taken into consideration in patch design process. This critical-site-tracking (CST) method is especially suitable for analyzing large 3D data sets to identify critical sites and indices related to the disease state under investigation

Table 1: Stroke volume and ejection fraction comparisons for three models considered. M1: pre-operation model with scar+ old patch; M2: conventional patch; M3: proposed small patch with aggressive trimming. Adjusted SV for M1 was obtained by including pulmonary regurgitation determined by CMR (Fig. 12). M4: small patch model with adjustment pressure condition to match post-operation CMR data.

Cases	Pre-Op Model (M1)	Pre-Op Model	Patch Model 1 (M2)	Patch Model 2 (M3)	CMR Data	Model 2 modified (M4)
	Old (large) Patch + Scar	+Pulmonary Regurgitation	Conv. Large Patch	Small Patch + Trimming	Post-Op actual data	Using post-op data
RVEDV(ml)	412.7		256.9	208.7	188.3	118.28
RVESV(ml)	254.9		162.1	123.2	115.0	115.65
SV (ml)	157.8	74.6 (outflow)	94.9	85.5	73.3	72.63
Ejection Fraction (%)	38.2	EF PR_{adj}: 18.1	36.9	41.0	38.9	38.6

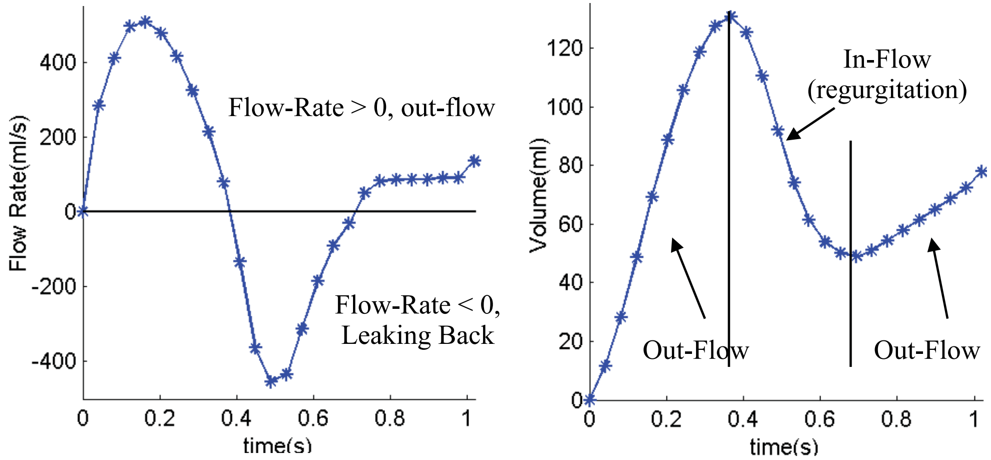
(a) CMR-Measured Average Flow Rate at the Pulmonary Valve

(b) CMR-Measured Accumulated Total Out-Flow at the Pulmonary Valve

Figure 12: CMR-measured flow rate at the outlet and accumulated out-flow volume at the pulmonary valve for the pre-operation model (M1).

[33]. Our results also shows that stress conditions around the patch are far more sensitive to patch variations and may serve as better indicators for comparative analysis in patch design (size, shape and material properties) and optimization process.

3.4 *Validation Using Pre- and Post-Operative Data*

Pre-operation data was used not only for determining the material parameters in the model, but also for validation of the model and computational results. RV pressure and volume data were used to determine patient-specific parameter values for material models to fit CMR RV volume data. The validated model matching pre-operation data (patient-specific RV/LV morphology, material parameters and pressure conditions) was used to perform patch-design simulations and predict post-operation RV cardiac function. Since the model was applied to the same patient, the pre- and post-operation ventricle tissue material properties should remain the same.

Actual surgery outcome may differ from computational predictions since there is a considerable distance between computational models and what the surgeon can accomplish in the operating room. Follow-up data was acquired six months after the surgery and compared with pre-operation computational predictions. This serves as the

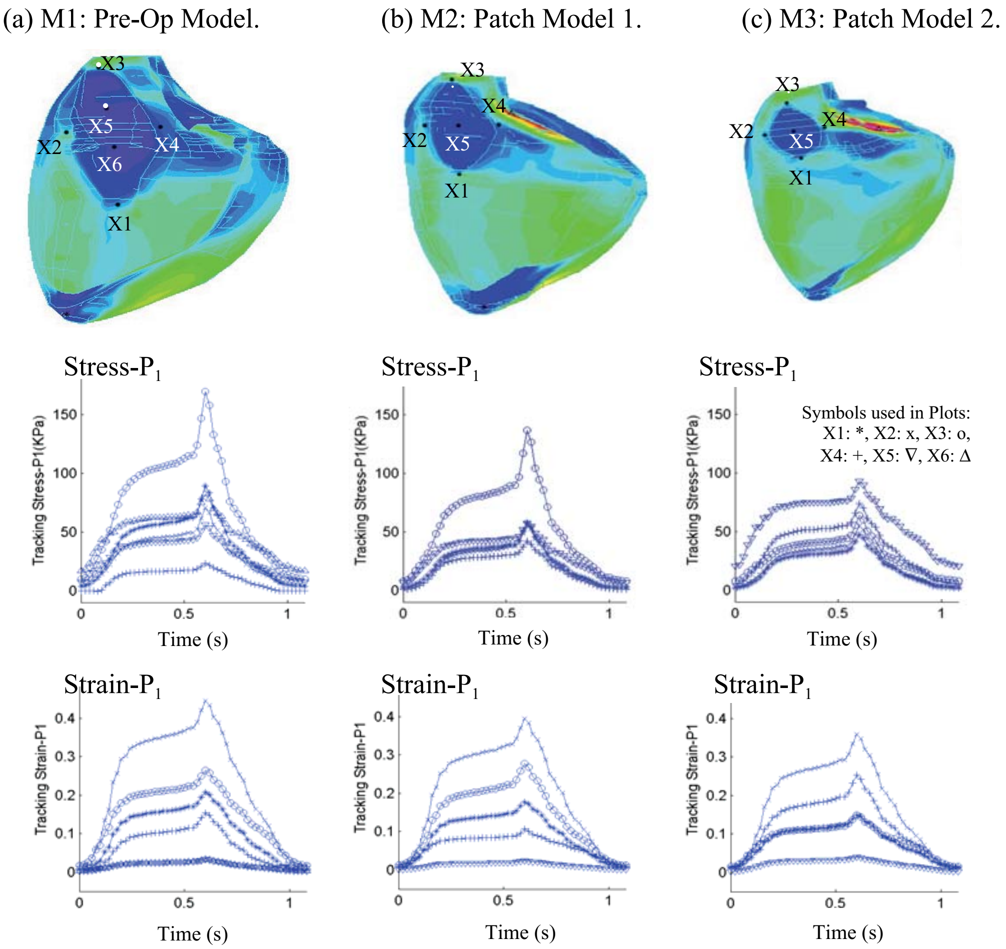
(a) M1: Pre-Op Model.
(b) M2: Patch Model 1.
(c) M3: Patch Model 2.

Figure 13: Stress-P_1/Strain-P_1 variations tracked at selected tracking points (marked on Strain-P_1 plots) locations for the three cases show that stress/strain levels in the patch area are considerably lower (> 50% for stress, > 20% for strain) from the pre-operation model to the other two models. Strain-P_1 distributions from the three models were used to show locations of tracking sites. Selected tracking points and marking symbols in the plots: X1: *, just below the patch (or scar for M1); X2: x, just next to the left of the patch; X3: o, just above the patch; X4: +, just next to the right of the patch; X5: ∇, at the center of the patch; X6: Δ, just below the patch (this is for pre-op model only).

final validation of our proposed surgical procedure and optimization process and provide valuable information for future improvements. Fig. 14 gives post-operation MR images of the same patient whose pre-operation data were used for our demonstration. The CMR-measured and computer-predicted (patch Model 2) RV volume curves are given by Fig. 14(c), and the error margin is 8.8%. Noticing the differences in the volume profile and the over-all over-estimation by Patch Model 2, pressure condition and material parameters were adjusted and new predicted RV volume had much improved accuracy (new predicted maximum volume: 188.28 ml, error < 0.01%; error for the entire cycle < 2%). SV and EF values are listed in Table 1 to compare with those from other models. This modification technique will be applied to future cases so that the first-time prediction accuracy can be improved. Data obtained and experience learned will be applied to subsequent patient surgery design. Our team and the optimization process will improve as more pre- and post-operative data analysis and optimizations are completed.

(a) Post-Op CMR Images (10 selected from 12 slices) from the Same Patient.

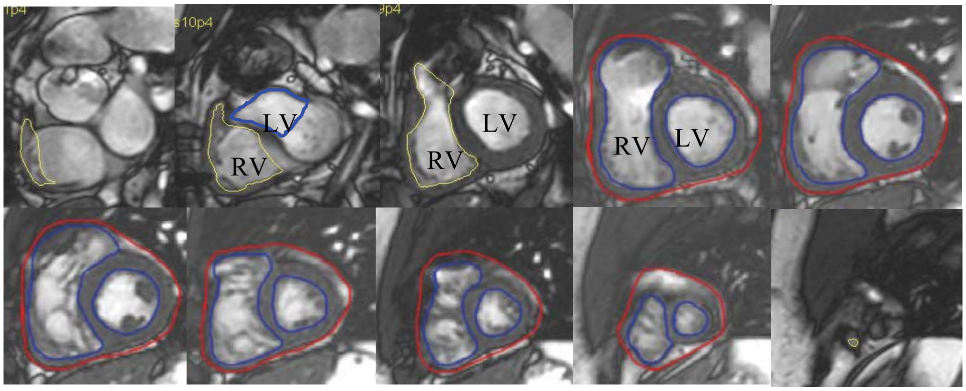

(b) Computational Pre- and Post-Op Pressure Conditions in RV.

(c) Computer-Predicted and CMR-Measured RV Volumes.

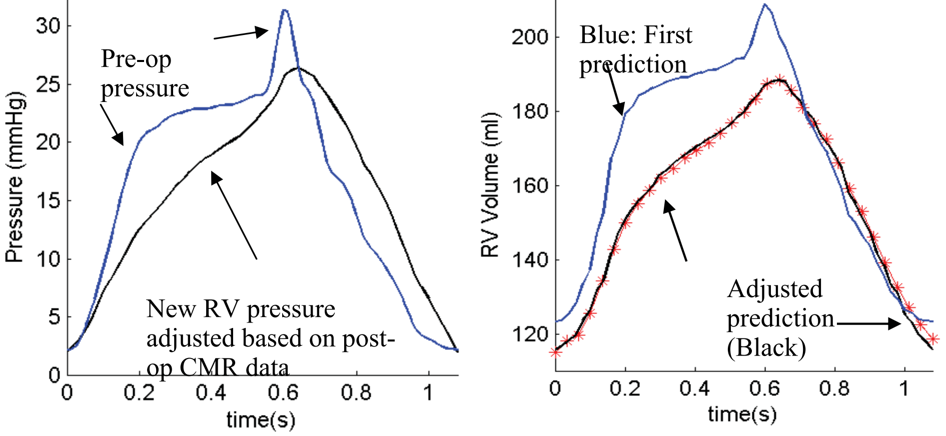

Figure 14: Validation by post-operation data. (a) Post-operation CMR images; (b) Computational pre- and post-operation pressure conditions in RV; (c) Comparison between measured RV volume and two computational predictions. Blue line: volume using pre-operation pressure (CMR max volume 188.3 ml, predicted volume 204.9 ml, error margin 8.8%); black line: volume using adjusted pressure condition to match post-operation CMR RV volume (new predicted volume 188.28 ml, error < 0.01%; error for the entire cardiac cycle < 2%).

4 Discussion

With the rapidly increasing number of late survivors of repair of tetralogy of Fallot, surgical management of patients with right ventricular dysfunction has become a major clinical challenge. The wide variability in clinical status, extent of right ventricular dilatation, scarring, and dysfunction at the time of presentation has resulted in disparate surgical results with pulmonary valve insertion alone [38]. The proposed multi-disciplinary approach of integrating innovative computational modeling, surgical procedures and noninvasive CMR techniques has the potential for improved outcome of RV remodeling surgical procedures associated with pulmonary valve replacement surgery. For the first time, patient-specific 3D computational RV/LV/Patch combination models with fluid-structure interactions and surgical procedure design will be developed to simulate blood flow and stress/strain in the right ventricle. Computational simulations will be used to supplement/replace empirical and often risky clinical experimentation, or even guide the design of new clinical trials to examine the efficiency and suitability of various reconstructive procedures in diseased hearts so that optimal design can be found. The proposed surgical procedures of right ventricular remodeling will be tested and optimized by computational simulations before the surgeon actually operates on the patient.

Several improvements can be added to our models in the future for better accuracy and applicability: a) Direct measurements of tissue mechanical properties will be very desirable for improved accuracy of our models; b) Mechanical Valve mechanics and pulmonary regurgitation. While exact valve motion and mechanics are not included in the current model, the valve opening/closing can be controlled and adjusted to simulate pulmonary regurgitation. Our model can be adjusted so that the outlet can be made partially open in the diastole period with proper pressure conditions specified to reach measured flow and RV volume variation data. c) Industrial patch materials can be used in the model for actual evaluations of different brands and product from different manufacturers. d) Active contraction model. Another way to add active contraction into our model is to introduce an external force field which is tied to fiber structure and orientations. The difficulty is that measurement and validation of the external force field are not currently available. Information obtained from animal models could be used as an approximate starting point [8, 9]. We expect that the SV and EF predictions by our current model and a heart model including active contractions will have the same accuracy.

5 Conclusion

Our preliminary results indicated that the active anisotropic RV/LV/Patch model with two-layer construction and fiber orientations provide considerable improvements in computational stress/strain predictions, compared to the previous passive isotropic models. Maximum Stress-P_1 value from passive and active anisotropic models were 149.6% and 121.2% higher than those from the passive isotropic model, respectively. Patient-specific MRI-based FSI models validated by pre-operation data have great potential to make accurate assessment of RV cardiac function and may be used to perform virtual surgeries to replace expensive and risky surgical experiments. The proposed small patch model with aggressive scar tissue trimming provided 11% improvement in RV function as measured by RV ejection fraction, and considerably lower (20-40% lower) stress level in the patch region, compared to the conventional patch. Scientifically, the 3D flow, RV stroke volume, ejection fraction, and 3D RV stress/strain distributions from participating patients and healthy volunteers will be adding to the current literature and form a database for future research and investigations.

Acknowledgement: This research was supported in part by NIH–HL63095 (PI: del Nido) and NIH-NHLBI 5P50HL074734 (PI: Geva; Co-Investigator: del Nido).

References

1. Axel, L. (2002) Annu. Rev. Biomed. Eng., 4, 321-347.
2. Bathe, K. J. (1996), Finite Element Procedures, (Prentice Hall, Inc. New Jersey).
3. Bathe, K. J., Eds, (2002) Theory and Modeling Guide, Vol I & II: ADINA and ADINA-F, (ADINA R & D, Inc., Watertown).
4. Berne, R. M., M. N. Levy, B. M. Koeppen, B. A. Stanton, (2004) Physiology, Fifth Edition, Mosby, Elsevier, St. Louis, MO.
5. Bloomgarden, D. C., Z. A. Fayad, V. A. Ferrari, B. Chin, M. G. Sutton, and L. Axel, (1997) Magn Reson Med. 37, 683-692.
6. Costa, K. D., Y. Takayama, A. D. McCulloch, J. W. Covell, (1999) Am J Physiol. 276(2 Pt 2), H595-607.
7. del Nido, P. J. (2006) Semin Thorac Cardiovasc Surg Pediatr Card Surg Annu. 29-34.
8. Guccione, J. M., K. D. Costa, A. D. McCulloch, (1995) J Biomech. 28(10), 1167-77.
9. Guccione, J. M., A. D. McCulloch, L. K. Waldman, (1991) J Biomech Eng. 113(1),42-55.

10. Guccione, J. M., G. S. Le Prell, P. P. de Tombe, W. C. Hunter, (1997) J Biomech. 30(2), 189-192.

11. Guccione, J. M., A.D. McCulloch, (1993) J Biomech Eng. 115(1), 72-81.

12. Guccione, J. M., L. K. Waldman, A. D. McCulloch, (1993) J Biomech Eng. 115(1), 82-90.

13. Holzapfel, G. A., T.C. Gasser, R. W. Ogden, (2000) Journal of Elasticity, 61, 1-48.

14. Holzapfel G. A., M. Stadler, C. A. J. Schulze-Bause, (2002) Annals of Biomedical Engineering, 30(6), 753-767.

15. Humphrey, J. D., (2002) Cardiovascular Solid Mechanics, Springer-Verlag, New York.

16. Hunter, P. J., A. J. Pullan, B. H. Smaill, (2003) Annu Rev Biomed Eng., 5, 147-77.

17. Kuehne, T. et al, (2004) Circulation. 110, 2010-2016.

18. May-Newman, K., A. D. McCulloch, (1998) Prog Biophys Mol Biol. 69(2-3), 463-81.

19. McCulloch, A. M. et al., (2007) Continuity 6 (a package distributed free by the National Biomedical Computation Resource), www.continuity.ucsd. edu.

20. McCulloch, A. M., L. Waldman, J. Rogers, J. Guccione, (1992) Critical Rev. in Biomedical Engineering, 20(5,6): 427-449.

21. Nash, M. P., P. J. Hunter, (2000) Journal of Elasticity, 61:113–141.

22. Peskin, C. S., (1975) Mathematical Aspects of Heart Physiology, Lecture Notes of Courant Inst. of Mathematical Sciences, New York.

23. Peskin, C. S., D. M. McQueen, (1992) Crit Rev Biomed Eng. 20(5-6), 451-459.

24. Rogers, J. M., A. D. McCulloch, (1994) J Cardiovasc Electrophysiol. 5(6), 496-509.

25. Saber, N. R., A. D. Gosman, N. B. Wood, P. J. Kilner, C. L. Charrier, and D. N. Firman, (2001) Annals of Biomech. Engng., 29, 275-283.

26. Sacks, M. S., C. J. Chuong, (1993) J Biomech Eng, 115:202-205.

27. Sanchez-Quintana, D., R. Anderson, S.Y. Ho, (1996) Heart, 76, 280-286.

28. Stevens, C., P. J. Hunter, (2003) Prog. in Biophysics & Molecular Biology, 82, 229-241.

29. Stevens, C., E. Remme, I. LeGrice, P. J. Hunter, (2003) J Biomech., 36(5), 737-48.

30. Takayama, Y., K. D. Costa, J. W. Covell, (2002) Am J Physiol Heart Circ Physiol. 282(4), H1510-20.

31. Tang, D., C. Yang, T. Geva, P. J. del Nido, (2007) J. of Biomech. Engineering, in press.

32. Tang, D., C. Yang, J. Zheng, P. K. Woodard, G. A. Sicard, J. E. Saffitz, and C. Yuan, (2004) Annals of Biomedical Engineering, 32(7), 947-960.

33. Tang, D., C. Yang, J. Zheng, P. K. Woodard, J. E. Saffitz, J. D. Petruccelli, G. A. Sicard, and C. Yuan, (2005) Annals of Biomed.l Engineering,33(12), 1789-1801.

34. Therrien, J., S.C. Siu, P.R. McLaughlin, et al., (2000) J Am Coll Cardiol. 36,1670-5.

35. Usyk, T. P., A. D. McCulloch, (2003) J Cardiovasc Electrophysiol., 14(10), S196-202.

36. Vetter, F. J., A. D. McCulloch, Annals of Biomech. Engng. 28, 781-792.

37. Vliegen, H. W., A. Van Straten, A. De Roos, A. A. Roest, P. H. Schoof, A. H. Zwinderman, J. Ottenkamp, E. E. Van Der Wall, M. G. Hazekamp, (2002) Circulation, 106:1703-1707.

38. Waien, S.A., P. P. Liu, B. L. Ross, W. G. Williams, G. D. Webb, P. R. McLaughlin. (1992) J Am Coll Cardiol. 20, 295-300.

39. Yang, C., D. Tang, I. Haber, T. Geva, P. J. del Nido, (2007) Computers & Structures, 85, 988-997.